CHAPTER 2

ANALYSIS OF GYROKLYSTRON AMPLIFIERS*

*Part of this work has been published as:

M. V. Swati, M. S. Chauhan, and P. K. Jain, "Time-Dependent, multimode interaction analysis of the Gyroklystron amplifier," *Phys. Plasmas*, vol. 23, no.8, pp. 083124 (1-8), 2016.

CHAPTER 2

ANALYSIS OF GYROKLYSTRON AMPLIFIERS

2.1. Introduction

Gyroklystron amplifiers capabilities to provide high power, high gain and moderate bandwidth make it as an attractive high power millimeter wave device [Barker and Schamiloglu (2001), Nusinovich (2004)]. Gyroklystrons have proven potential applications in numerous upcoming applications, such as, high-resolution radars, linear particle accelerators, plasma heating and magnetic resonance imaging, etc. [Chu (2004), Gold and Nusinovich (1997)]. Historically, the first gyroklystron operation in the fundamental harmonic was tested in Russia in the year 1967 and reported in the literature in the year 1978 [Andronov *et al*. (1978)]. The attractive feature of this experiment is its high efficiency. The first experimental operation of a second harmonic gyroklystron amplifier was developed by USA in 1977. A three-cavity X-band gyroklystron amplifier was developed generating output pulsed power of 20kW, an efficiency of 8% and corresponding gain of 10dB [Jory (1977)]. Afterwards, the research at the Institute of Applied Physics (IAP), Russia developed gyroklystron for radar applications in the late 1990s. In their first experiment, they were able to produce an output power of 125kW with 17% efficiency, 15dB gain and 0.1% bandwidth with 60kV beam voltage and 13.5A beam current using two cavities at 35GHz [Antakov *et al*. (1994)]. Later on, they demonstrated experimentally two-cavity gyroklystron with higher beam voltage and beam current to enhance gyroklystron output power and efficiency. In the process of experimental studies of this amplifier, pulsed output power of 260kW was achieved with an efficiency of 18%,

corresponding gain of 17dB and a bandwidth of amplified frequencies of 0.1% [Zasypkin *et al*. (1996)]. After that, results of an experimental study of a three-cavity Ka-band gyroklystron amplifier producing 300kW peak power with 22% efficiency, a saturated gain of 22dB and about 0.12% bandwidth has been reported by the IAP [Gachev *et al*. (2002)]. Since that, during 1998-2002, IAP efforts were concentrated on the development and testing of a Ka-band second harmonic gyroklystron operating with PMS. A number of analytical research works have been reported in the literature for the design and analysis of the fundamental harmonic gyroklystron amplifier. Different approaches have been incorporated which led to the considerable physical insight into the principle of operation of the gyroklystrons. To demonstrate and investigate the RF beam-wave interaction behaviour of the gyroklystron amplifier, the linear and nonlinear analyses are developed. There are primarily two approaches used for modeling and analyzing the gyroklystron circuit which depends on the axial field profile. Firstly, non self-consistent approach in which a fixed profile function such as sinusoidal function for closed cavities and Gaussian function for open cavities is used to describe the RF field in the RF cavities of the gyroklystrons, i. e., the effect of the electron beam on the RF profile is neglected [Tran *et al*. (1986), Nusinovich (2004)]. As per the literature, scattering matrix method is an efficient technique and is widely used for the modeling and design of the gyroklystron amplifier, where the exact, real time cold-field profile is desired inside the cavities. These field profiles are computed non self-consistently and can be employed mainly for the experimental designing of the device [Calame *et al*. (1999), Danly *et al*. (2000), Garven *et al*. (2000)]. In addition, scattering matrix technique is also very much helpful in the analysis of the complex cavities (i. e., stepped cavities, irregular radius cavities etc.) [Neilson *et al*. (1989)]. There are several numerical codes, such as CASCADE [Ives *et al*.

(2003)], to compute these field profiles on the basis of scattering matrix method. Secondly, self-consistent approach, in which the cavity field profiles do not retain to its cold (electron beam absent) values and completely evolve according to the interaction with the electron beam. In this approach, the equations of motion for the electrons are solved simultaneously with the help of the field equations [Salop and Caplan (1986), Geng *et al*. (2004), Luo *et al*. (2005), Wang *et al*. (2008), Jianhua *et al*. (2011)]. These gyroklystron models are restricted using certain assumptions, i. e., ignoring space charge effects, complete isolation between the RF cavities, uniform guiding magnetic field to make the analysis simpler and to reduce the computation time. In most of the literature, the effect of velocity spread is not taken into consideration while carrying out the analysis [Tran *et al*. (1986), Geng *et al*. (2004), Nusinovich (2004), Luo *et al*. (2005), Wang *et al*. (2008), Jianhua *et al*. (2011)] whereas included by [Salop and Caplan (1986)], and [Shou-Xi *et al*. (2012)]. In most of the reported work, the time-independent single mode operation is considered in each cavity except in [Luo *et al*. (2005)] in which a semi-multimode approach is used to analyze the beam-wave interaction behavior in the operating mode as well as the other modes with the same azimuthal index but different radial indices. But, for the gyroklystron amplifier, significant amount of work is not reported in the literature for the time-dependent multimode operation of the device which gives the concept of mode competition in more real time scenario. Nowadays, time-dependent simulation and analysis of the electromagnetic fields is essential for the detailed description of the beam-wave interaction mechanism.

In the development of high power and high efficiency gyroklystron amplifier, mode purity is one of the important factor that affect the interaction of input RF signal and electron beam. To achieve higher power at higher frequencies, gyroklystron has to be

necessarily operated at the higher order modes, which in turn increase the size of the interaction structure and reduces the problem of beam interception and wall heating, which mainly occurs due to the miniaturization of interaction structures at these frequencies. However, the device operation at higher order modes increases the mode density in the cavity which affects the performance of the device, such as, efficiency, and desired operating modes. Additionally, for such higher frequency of operation, larger magnetic field is required for the fundamental mode of operation which limits the application of gyroklystron amplifier as a millimeter-wave source and makes the system heavy and difficult to achieve. The attractive alternative is to operate the device at a harmonic of the operating frequency so that the magnetic field requirement is reduced by the harmonic number *s*. Such magnetic field can also be easily produced by the permanent magnetic systems (PMS). However, efficiency decreases with the increase in the harmonic number, hence; there is a considerable interest in the second harmonic gyroklystron amplifiers. Moreover, higher harmonic modes are also difficult to excite because of mode competition from the nearby higher harmonic competing modes as well as the fundamental harmonic modes [Brand *et al.* (1992), Liu and Borie (2000)]. Therefore, the study of the multimode interaction becomes important for the gyroklystron amplifiers operating at its harmonics. Several methods have been introduced to suppress the unwanted modes like loading the drift tubes with dielectrics, modifying the output section to reduce the reflections off the nonlinear up taper [Latham (1990)] or by employing the coaxial cavities [Tiwari and Lawson (2007)] in the gyroklystron.

In 1986, the time-independent nonlinear analysis of the gyroklystron amplifier was reported [Salop and Caplan (1986)] by extending the basic analytical approach followed for the gyrotron oscillators [Fliflet *et al*. (1982)]. In the similar fashion, the time-dependent

multimode nonlinear analysis has been developed for the gyroklystron amplifier by extending the time-dependent multimode nonlinear formulation as developed for gyrotron oscillators by Fliflet *et al.* (1981). In addition, field profiles in the cavities have been computed self-consistently. The space charge effect and the effect of a velocity spread on the beam wave interaction in the cavities are assumed to be small and hence neglected. The present time-dependent multimode analysis is used to predict the output behavior of the device in terms of RF output power, efficiency, gain and bandwidth and to observe the mode competition inside the cavity. To validate the developed self-consistent time-dependent multimode analysis, the design specifications of an experimental three-cavity Ka-band second harmonic gyroklystron amplifier has been considered [Antakov *et al*. (2011)].

This chapter of the thesis is organized as follows. In Section 2.2, the multimode nonlinear analysis including the time-dependent description of the electromagnetic fields and the electron motion expressions are described. The design parameters considered for the analysis are discussed in Section 2.3. Computational results obtained by the present time-dependent multimode nonlinear analysis are described in Section 2.4. and validated with the earlier reported experimental values [Antakov *et al.* (2011)]. Further, the sensitivity of RF output power, efficiency, and gain to the various device parameters are also discussed. The conclusions are drawn in Section 2.5.

2.2. Nonlinear Analysis

There has been a steady progress of both analytical and experimental work for the gyroklystron amplifiers. Theoretical analysis helps the researchers in in-depth understanding of the physics behind the operation of the device by taking into consideration

practical constraints without fabricating the actual device. For the analysis of a gyroklystron amplifier, both linear and nonlinear analyses (large signal analysis) are used and they are supposed to perfectly verify each other in the linear interaction region. Linear analysis is used for the initial study of the device without taken into consideration the real time parameters. The linearization process assumes that there is no interaction between orthogonal EM modes in the linear regime. In other words, the nonlinear sets of differential equations are linearized to study the starting conditions of the device. Hence, the linear analysis is used to predict the start oscillation conditions, linear gain, and launching loss which can provide guidelines for the design of a stable device. On the other hand, the nonlinear analysis is used to predict output power, efficiency, saturation gain, and phenomenon of electron cross-over and de-bunching, hence providing better understanding of the saturation mechanism and thereby provide complete analysis of the overall structure. There are two approaches of analyzing the non-linear interaction between the gyrating electrons and EM fields. Firstly, the self-consistent approach in which modification of an axial structure of the field by the high frequency component of the electron current density is taken into consideration [Salop and Caplan (1986), Jianhua *et al.* (2011)]. Secondly, the non self-consistent approach in which an axial field profile is fixed, such that the electron beam cannot modify it significantly [Tran *et al.* (1985)]. The purpose of our work is to develop and apply a self-consistent nonlinear multimode formulation, which is simultaneously adoptable for efficient numerical simulations and applicable for the analytical considerations.

2.2.1. Time-Dependent Multimode Interaction Analysis

In carrying out a simple and more generalized self-consistent multimode time dependent nonlinear analysis, the following procedures are employed. The ensemble of electrons which includes the sufficient number of electrons is injected into the input cavity which provides the longitudinal velocity distribution and for each electron velocity; a uniform distribution in gyration phase angle is represented. The generalized coupled nonlinear equations of motion of electrons are typically derived for the calculation of momentum and phase of the particles and RF electric field profile wave equation by considering the cumulative effect of all possible modes in the cavity. These equations are then solved self-consistently for each cavity by satisfying the appropriate boundary conditions for the particle momentum and phases and the field profile.

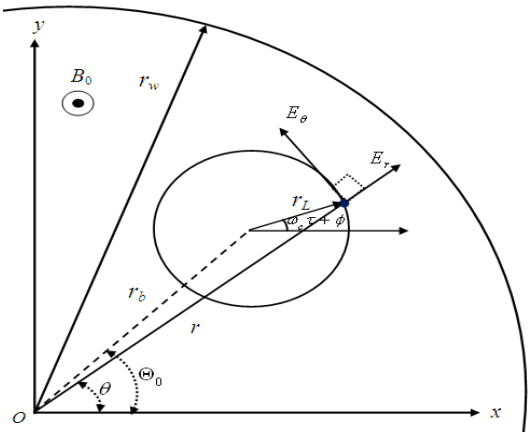

Figure. 2.1: Arrangement of the gyrating electrons in Larmor orbit in the Cartesian as well as cylindrical coordinate systems.

Hence, in the present analysis developed for gyroklystrons, the momentum and phase are obtained for each cavities of the gyroklystron amplifier such that the particle momentum and phases entering the adjacent cavity are considered as those at the exit of the first cavity except for the phase change which mainly occurs in the field-free drift tube. The basic formulation used in the present analysis follows the derivation of time-dependent

nonlinear analysis as described for gyrotron oscillators [Fliflet *et al*. (1991)] as described below:

I. Adiabatic equation for electron momentum and phase

In the analysis, a thin gyrating beam of electrons is considered. The arrangement of gyrating electron beam in a cylindrical cavity with all its coordinates is shown in Fig. 2.1. Electrons move on a helical path gyrating about the guiding center radius R_b.

Lorentz's force equation governing motion of electrons in the presence of perturbing RF fields is given by:

$$\frac{dp}{dt}+\frac{|e|}{\gamma m_e}P\times B_0=-|e|\left(E+\frac{1}{\gamma m_e}P\times B_0\right)\equiv a' \quad , \tag{2.1}$$

where, B_0 is the applied magnetic field ($B_0 = B_0\hat{z}$), p is the momentum of the electron, E and B are the RF electric and magnetic fields, and γ is the relativistic mass factor defined as $\gamma = [1 + p^2/(m_e c)^2]^{1/2}$. Electrons' interaction with the RF fields result in perturbations in their momentum and phase, i. e., their momentum and phase deviate from the normal values they would have possessed if there were no interaction. To facilitate tracking of changes in the momentum and phase of electrons and with an observation on the most suitable co-ordinate system, the cylindrical co-ordinate system in this context is considered. Hence, the representing transverse momentum can be written in the form

$$p_x + ip_y = ip_t \exp\left[i\left(\omega_c\tau+\phi\right)\right] \quad , \tag{2.2}$$

where, p_t and ϕ are the slow time scale magnitude and phase of transverse momentum. The term slow time scale indicates those temporal derivatives of the two, momentum and phase, are quiet less than operating frequency (ω_0) or the reference cyclotron frequency (ω_c). Before interaction, equation (2.2) can be written as:

$$p_x + ip_y = i\,p_t \exp[i(\omega_c \tau + \phi_0)] \quad , \tag{2.3}$$

where, ϕ_0 and p_t are the initial gyro-phase of an electron in a beamlet and transverse momentum, respectively.

On simplifying equation (2.1), it can be expressed as,

$$a_x' + ia_y' = \frac{dp_x}{dt} + i\frac{dp_y}{dt} + \frac{\gamma_0}{\gamma}\omega_c \left(p_y - ip_x \right) \quad , \tag{2.4}$$

and $$a_x' - ia_y' = \frac{d\,p_x}{dt} - i\frac{d\,p_y}{dt} + \frac{\gamma_0}{\gamma}\omega_c (p_y + i\,p_x) \quad . \tag{2.5}$$

Differentiating equation (2.1) and taking complex conjugates, it can obtained as,

$$\frac{d\,p_x}{dt} + i\frac{d\,p_y}{dt} = i\,p_t \exp[i(\omega_c \tau + \phi)](i\omega_c + i\frac{d\phi}{dt}) + i\exp[i(\omega_c \tau + \phi)]\frac{d\,p_t}{dt} \quad , \tag{2.6}$$

and $$i\,p_x - p_y = -p_t \exp[i(\omega_c \tau + \phi)] \quad . \tag{2.7}$$

Substituting the above expressions into equations (2.4) and (2.5), it can be written as,

$$[a_x' + ia_y']\exp[-i(\omega_c \tau + \phi)] = -p_t(\omega_c + \frac{d\phi}{dt}) + i\frac{d\,p_t}{dt} + \frac{\gamma_0}{\gamma}\omega_c\, p_t \quad , \tag{2.8}$$

and $$[a_x' - ia_y']\exp[i(\omega_c \tau + \phi)] = -p_t(\omega_c + \frac{d\phi}{dt}) - i\frac{dp_t}{dt} + \frac{\gamma_0}{\gamma}\omega_c p_t \quad . \tag{2.9}$$

Addition and subtraction of the above equations lead to the following:

$$\frac{d\,p_t}{dt} = \frac{i}{2}\{(a_x' - ia_y')\exp[i(\omega_c \tau + \phi)] - (a_x' + ia_y')\exp[-i(\omega_c \tau + \phi)]\} \quad , \tag{2.10}$$

$$\frac{d\phi}{dt} = -\frac{1}{2}\{(a_x' - ia_y')\exp[i(\omega_c \tau + \phi)] + (a_x' + ia_y')\exp[-i(\omega_c \tau + \phi)]\} \times \frac{1}{p_t} - \omega_c(1 - \frac{\gamma_0}{\gamma}) \quad , \tag{2.11}$$

and $$\frac{d\,p_z}{dt} = a_z' \quad . \tag{2.12}$$

It is considered that the electron beam interacts with one or more competing modes closely spaced in the cavity. In terms of cylindrical coordinates, the total transverse electric and magnetic field component (in practice, the field amplitude is obtained by evaluating the real part) is given by:

$$E_t = \mathrm{Re}\left\{ \sum_{n=1}^{N} A_n\{z,t\} e_n\{r,\theta\} e^{-i\omega_0 t} \right\} \quad , \tag{2.13}$$

$$B_t = \mathrm{Re}\left\{ \sum_{n=1}^{N} -\frac{i}{\omega_0}\frac{\partial}{\partial z} A_n\{z,t\} b_n\{r,\theta\} e^{-i\omega_0 t} \right\} \quad , \tag{2.14}$$

where, $e_n\ (=\hat{z}\times\nabla_t\psi_n)$ and $b_n\ (=-\nabla_t\psi_n)$ are the vector functions. ψ_n is scalar or membrane function of n^{th} mode that satisfies the Helmholtz equation. $A_n\ \{z, t\}$ is the field amplitude. N is the number of modes that are assumed to be interacting. The axial component can be given by:

$$B_z = \mathrm{Re}\left\{ \sum_{n=1}^{N} \frac{ik_t^2}{\omega_0} A_n\{z,t\}\psi_n e^{-i\omega_0 t} \right\} \quad , \tag{2.15}$$

where, ψ_n is the membrane function given by

$$\psi_n\{r,\theta\} = C_{m_n l_n} J_{m_n}\left\{k_{m_n l_n} r\right\} \exp[i m_n \theta] \quad ,$$

and

$$C_{m_n l_n} = \frac{1}{\sqrt{[\pi(x'^2_{m_n l_n} - m_n^2)]} \times J_{m_n}\left\{x'_{m_n l_n}\right\}} \quad . \tag{2.16}$$

After defining the RF fields, the components a'_x, a'_y, a'_z can be determined subsequently. As the cylindrical co-ordinate system is intended to use, the two transverse components a'_x, and a'_y can be defined in terms of a'_r and a'_θ as:

$$a'_x = a'_r \cos\theta - a'_\theta \sin\theta, \text{ and } a'_y = a'_r \cos\theta + a'_\theta \sin\theta \quad . \tag{2.17}$$

To determine the components a_r', a_θ', and a_z', the momentum vector P in the equation (2.1) defined in cylindrical coordinate system as:

$$P = p_t \cos(\varphi-\theta)\hat{r} + p_t \sin(\varphi-\theta)\hat{\theta} + p_z \hat{z} \text{ , where, } \varphi = \omega_c \tau + \phi \quad . \tag{2.18}$$

Now, $B_t = \mathrm{Re}\left\{\sum_{n=1}^{N} \frac{i}{\omega_0}\frac{\partial}{\partial z} A_n\{z,t\}\nabla_t \psi_n e^{-i\omega_0 t}\right\}$ and $E_t = \mathrm{Re}\left\{\sum_{n=1}^{N} A_n\{z,t\}\hat{z}\times\nabla_t\psi_n e^{-i\omega_o t}\right\}$. (2.19)

Since, $b_n = -\nabla_t\psi_n = -\frac{\partial\psi}{\partial r}\hat{r} - \frac{1}{r}\frac{\partial\psi}{\partial\theta}\hat{\theta}$, and $e_n = \hat{z}\times\nabla_t\psi_n = -\frac{1}{r}\frac{\partial\psi}{\partial\theta}\hat{r} + \frac{\partial\psi}{\partial r}\hat{\theta}$, therefore, the components of magnetic and electric fields can be obtained as:

$$B_r = \mathrm{Re}\left\{\sum_{n=1}^{N} C_{m_n l_n}\frac{i}{\omega_0}\frac{\partial}{\partial z} A_n\{z,t\} k_{m_n l_n} J'_{m_n}\left\{k_{m_n l_n} r\right\}\exp[i(m_n\theta-\omega_0 t)]\right\} \quad , \tag{2.20}$$

$$B_\theta = \mathrm{Re}\left\{\sum_{n=1}^{N} C_{m_n l_n}\frac{-1}{\omega_0}\frac{\partial}{\partial z} A_n\{z,t\}\frac{m_n}{r} J_{m_n}\left\{k_{m_n l_n} r\right\}\exp[i(m_n\theta-\omega_0 t)]\right\} , \tag{2.21}$$

$$B_z = \mathrm{Re}\left\{\sum_{n=1}^{N} C_{m_n l_n}\frac{i}{\omega_0} A_n\{z,t\} k_t^2 J_{m_n}\left\{k_{m_n l_n} r\right\}\exp[i(m_n\theta-\omega_0 t)]\right\} \quad , \tag{2.22}$$

$$E_r = \mathrm{Re}\left\{\sum_{n=1}^{N} -C_{m_n l_n}\frac{i m_n}{r} A_n\{z,t\} J_{m_n}\left\{k_{m_n l_n} r\right\}\exp[i(m_n\theta-\omega_0 t)]\right\} \quad , \tag{2.23}$$

and $$E_\theta = \mathrm{Re}\left\{\sum_{n=1}^{N} C_{m_n l_n} k_{m_n l_n} A_n\{z,t\} J'_{m_n}\left\{k_{m_n l_n} r\right\}\exp[i(m_n\theta-\omega_0 t)]\right\} \quad . \tag{2.24}$$

Now, on evaluating,

$$P\times B = [p_t \sin(\varphi-\theta)B_z - p_z B_\theta]\hat{r} - [p_t\cos(\varphi-\theta)B_z - p_z B_r]\hat{\theta}$$

$$+\hat{z}[p_t\cos(\varphi-\theta)B_\theta - p_t\sin(\varphi-\theta)B_r] \quad . \tag{2.25}$$

therefore,

$$a_r' = -|e|(E_r + v_t\sin(\varphi-\theta) - v_z B_\theta \quad ,$$

$$a'_\theta = -|e|(E_\theta - v_t \cos(\varphi - \theta) + v_z B_r) \quad ,$$

$$a'_z = -|e|(v_t \cos(\varphi - \theta) B_\theta - v_z \sin(\varphi - \theta) B_r) \quad ,$$

$$a'_x = a'_r \cos\theta - a'_\theta \sin\theta \text{, and } a'_y = a'_r \cos\theta + a'_\theta \sin\theta \quad . \tag{2.26}$$

Taking simplest expression, a'_z, from the above, the following expression can be obtained after algebraic simplification as:

$$a'_z = -|e| v_t \,\mathrm{Re}\left\{ \sum_{n=1}^{N} \frac{C_{m_n l_n} k_{m_n l_n}}{\omega_0} \frac{\partial}{\partial z} A_n\{z,t\} [J_{m_n - 1}\{k_{m_n l_n} r\} \exp[i(m_n - 1)\theta - \omega_0 t + i\varphi] \right.$$

$$\left. + J_{m_n + 1}(k_{m_n l_n} r) \exp[i(m_n + 1)\theta - \omega_0 t - i\varphi] \right\} \quad . \tag{2.27}$$

Taking account the finiteness of the Larmor radius of the beamlet, the RF-electron interaction from the co-ordinate system centered at the centre of beamlets considered, rather than coordinate system centered along axis of the cavity. This co-ordinate transformation can be performed using Graf's addition theorem [Basu (1996), Winternitz *et al*. (2001)]. It is a special case of a general addition theorem, called Neumann's addition theorem, can be expressed in the following form:

$$C_\nu\{\eta R_{jl}\} e^{i\nu(\theta_j - \vartheta_{jl})} = \sum_{\mu=-\infty}^{\infty} C_{\nu+\mu}\{\eta R_{jl}\} J_\mu\{\eta r_l\} e^{[i\mu(\pi - \theta_l + \vartheta_{jl})]} \quad , \; j \neq l \quad , \tag{2.28}$$

where, C_ν can be represented in any form of the Bessel functions J_ν, I_ν, Y_ν, K_ν, $H_\nu^{(1)}$, and $H_\nu^{(2)}$. (r_ν, θ_ν) and (r_l, θ_l) are polar coordinates centered at two different positions with global coordinates O_j, O_l. (R_{jl}, ϑ_{jl}) are the polar coordinates of O_l with respect to O_j. This expression is valid only provided that $r_l < R_{jl}$ (although this restriction is unnecessary if $C = J$ and ν is an integer). The right hand side of the equation (2.27) can be written in suitable form to apply the Graf's theorem as:

$$a_z' = |e| v_t \,\mathrm{Re}\left\{\sum_{n=1}^{N} \frac{C_{m_n l_n}}{\omega_0} \frac{\partial}{\partial z} A_n\{z,t\} e^{-i\omega_0 t} [e^{i(m_n-1)\theta_0 + i\varphi} J_{m_n-1}\{k_{m_n l_n} r\} \exp[i(m_n-1)(\theta-\theta_0)]\right.$$

$$\left. + J_{m_n+1}\{k_{m_n l_n} r\} \exp[i(m_n+1)\theta - \omega_0 t - i\varphi]\right\} \quad . \tag{2.29}$$

After transformation to the new co-ordinate system using a fore-mentioned theorem, the following changes occur in the above equation:

$$\sum_{\mu=-\infty}^{\infty} J_{m_n-\mu}\{k_{m_n l_n} R_b\} J_{-\mu+1}\{k_{m_n l_n} r_L\} e^{-i(\mu-1)(\pi/2-\varphi+\theta_0)},$$

and $\frac{dp_x}{dt} + i\frac{dp_y}{dt} = ip_t \exp[i(\omega_c\tau+\phi)](i\omega_c + i\frac{d\phi}{dt}) + i\exp[i(\omega_c\tau+\phi)]\frac{dp_t}{dt}$ .respectively.

To obtain the slow-time scale equations, we can neglect all of the harmonics and imposing single harmonic interaction condition, i. e., $\mu = s$, for which $s\omega_c \approx \omega$ where, s is the harmonic number and replacing φ by $\omega_c\tau + \phi$, it can be written as:

$$\frac{dp_z}{dt} = a_z' = |e| v_t \,\mathrm{Re}\left\{\sum_{n=1}^{N} \frac{C_{m_n l_n}}{\omega_0} \frac{\partial}{\partial z} A_n\{z,t\} [(-i)^{s-1} J_{m_n-s}\{k_{m_n l_n} R_b\} \frac{\partial J_s\{k_{m_n l_n} r_L\}}{\partial r_L} e^{-i\Lambda}]\right\} \quad , \tag{2.30}$$

where, $\Lambda = (\omega_0 - s\omega_c)\tau + \omega_0 t_0 - s\phi - (m_n - s)\theta_0$,

and $r_L = u_t/\omega_0$.

r_L is the Larmor radius. Following similar procedure:

$$\frac{dp_t}{dt} = -|e| \mathrm{Re}\left\{\sum_{n=1}^{N} \frac{C_{m_n l_n}}{\omega_0} \left[\omega_0 A_n\{z,t\} + iv_z \frac{\partial}{\partial z} A_n\{z,t\}\right] \times \left[(-i)^{s-1} J_{m_n-s}\{k_{m_n l_n} R_b\} \frac{\partial J_s\{k_{m_n l_n} r_L\}}{\partial r_L} e^{-i\Lambda}\right]\right\},$$

(2.31)

$$\frac{d\Lambda}{dt} = \frac{s|e|}{p_t}\mathrm{Re}\left\{\sum_{n=1}^{N}\frac{C_{m_n l_n}}{\omega_0} i[\omega_0 A_n\{z,t\} + iv_z\frac{\partial}{\partial z}A_n\{z,t\} - \frac{k_{m_n l_n}^2}{s\omega_c\gamma_0}A_n\{z,t\}]\right.$$

$$\left.\times[(-i)^{s-1}J_{m_n-s}\{k_{m_n l_n}R_b\}\frac{s\partial J_s\{k_{m_n l_n}r_L\}}{\partial r_L}e^{-i\Lambda}]\right\} + \omega_c\left(\frac{\omega_0}{\omega_c} - s\frac{\gamma_0}{\gamma}\right) \quad . \qquad (2.32)$$

Hence, finally the expressions for the momentum and phase of the particles are obtained as [Fliflet *et al*. (1991)],

$$\frac{dp_t}{d\bar{z}} = -\frac{\gamma}{p_z}\sum_{n=1}^{N} fnJ_s'\{\bar{k}_{nt}\bar{r}_L\}\mathrm{Re}\left\{\left[h + i\frac{p_z}{\gamma\omega_0}\frac{dh}{d\bar{z}}\right]e^{-i\left(\left[\Lambda+\bar{\psi}_n\right]+\left(m_n-s\right)\theta_0\right)}\right\} \quad , \qquad (2.33)$$

$$\frac{d\Lambda}{d\bar{z}} = \bar{\omega}_0\left[1 - \frac{s\bar{\omega}_c}{\bar{\omega}_0\gamma}\right] - \frac{s\gamma}{p_z p_t}\sum_{n=1}^{N} f_n\frac{sJ_s'\{\bar{k}_{nt}\bar{r}_L\}}{\bar{k}_{nt}\bar{r}_L}$$

$$\times\mathrm{Re}\left\{\left[h + i\frac{p_z}{\gamma\bar{\omega}_0}\frac{dh}{d\bar{z}} - \frac{\bar{\omega}_{n0}^2 p_t^2}{s\bar{\omega}_c\bar{\omega}_0\gamma}h\right]e^{-i\left[\Lambda+\bar{\psi}_n\right]+\left(m_n-s\right)\theta_0}\right\} \quad , \qquad (2.34)$$

and $$\frac{dp_z}{d\bar{z}} = \frac{p_t}{p_z\bar{\omega}_0}\sum_{n=1}^{N} fnJ_s'\{\bar{k}_{nt}\bar{r}_L\}\mathrm{Re}\left[i\frac{dh}{d\bar{z}}e^{-i\left[\Lambda+\bar{\psi}_n\right]+\left(m_n-s\right)\theta_0}\right] \quad . \qquad (2.35)$$

where, γ is updated as $\gamma = [1 + p_t^2 + p_z^2]^{1/2}$. The linearized mode phase parameter can be written as:

$$\bar{\psi}_n\{z\} = \psi_n\{t_0\} + \left.\frac{d\psi_n}{dt}\right|_{t_0} z/v_z \quad .$$

Variables with bar represent the normalized quantities and are given as $\bar{r}_L = r_L/R_w$, $\bar{\omega}_c = \omega R_w/c$, $\bar{k}_{nt} = k_{nt}R_w$, $\bar{z} = z/R_w$, $\bar{\omega}_0 = \omega_0 R_w/c$.

Since the electromagnetic signal is applied to the operating mode, therefore; for the operating mode, the initial mode amplitude at the input cavity is given by [Fliflet *et al*. (1991)]:

$$f_n = F_n \gamma_0 \beta_{\perp 0}^{4-s} \left(\frac{2^{s-1} s!}{s^s} \right) x'_{m_n l_n} \quad , \tag{2.36}$$

where, F_n is the normalized field amplitude used in the gyroklystron analysis and is expressed as [Joye *et al*. (2004)]:

$$F_n = \frac{E_0 \beta_{\perp 0}^{s-4}}{B_0 c} \left(\frac{s^{s-1}}{2^{s-1}\, s!} \right) J_{m_n \pm s} \left\{ k_{nt} R_b \right\} \quad . \tag{2.37}$$

Here, R_b is the beam radius, the electric field amplitude E_0 for a cylindrical cavity can be calculated in terms of RF input power P_{in} and quality factor Q as [Tran *et al*. (1986)]:

$$E_0 = \sqrt{\frac{Q P_{in}}{\omega_0 \varepsilon_0 \pi L}} \frac{2}{R_w \left| J_{m_n} \left\{ x'_{m_n l_n} \right\} \right|} \quad . \tag{2.38}$$

The competing modes behave as noise for the gyroklystron amplifier, therefore; the initial mode amplitude for the competing modes at the input cavity can be calculated as [Fliflet *et al*. (1991)]:

$$f_n = \frac{|e|}{m_e c^2} x'_{m_n l_n} C_{m_n l_n} J_{m_n - s} \left\{ k_{nt} R_b \right\} \quad . \tag{2.39}$$

a) Axial field profile function $h\{\bar{z}\}$***:***

There are two principle approaches for analyzing the gyroklystron circuit which mainly depend upon the RF axial field profile $h\{\bar{z}\}$. In the first approach, the cold-cavity RF electric field profile $h\{\bar{z}\}$ in each cavity can be evaluated using the scattering matrix formulation. The formulation follows the assumption that cavity field profile remains unaltered in the presence of the electron beam, i. e., retains its cold-cavity profile throughout the analysis. This approach is not fully self-consistent [Calame *et al*. (1999), Danly *et al*. (2000)]. Secondly, the self-consistent approach in which the cavity field profiles does not retain to its cold (electron beam absent) values and completely evolve

according to the interaction with the electron beam. In this approach, the axial field profile is obtained by solving the Vlasov-like expression. This profile is known as self-consistent field profile [Calame *et al*. (1999), Danly *et al*. (2000)]. The present analysis utilizes the second approach to compute the field axial profile in the cavity.

In the input cavity, the interaction between the RF wave and beam particles is small enough and the particles (electrons) are uniformly distributed. Hence, simple sinusoidal profile function is used to solve the momentum and phase equations and is given as [Geng *et al*. (2006)]:

$$h\{\bar{z}\} = \sin\{\bar{k}_z \bar{z}\} \ , \quad \text{where,} \quad \bar{k}_z = \pi / \bar{L} \ . \quad \text{For Input/Driver cavity (closed cavity).}$$

However, as the beam particles travel from input to the buncher cavity and then reach up to the output cavity, the beam-wave interaction becomes stronger and modifies the axial mode profile. Thus in the succeeding cavities, the field profile is determined self-consistently using the modified Vlasov equation [Salop and Caplan (1986)]:

$$\left[\frac{d^2}{d\bar{z}^2} + \bar{\omega}_0^2\left(1 - \frac{i}{Q} - \bar{k}_{nt}^2\right)\right] h = -i\mu\bar{\omega}_0 I_b \bar{k}_{nt} C_{m_n l_n} J_{m_n - s}\left\{\bar{k}_{nt}\bar{R}_b\right\}$$

$$\times \frac{1}{2\pi}\int_0^{2\pi} d\Lambda_0 \frac{\bar{v}_t}{\bar{v}_z} J_{s-1}\left(\bar{k}_{nt}\bar{p}_t / \bar{\omega}_c\right)\exp\left(is\Lambda\right) \quad , \qquad (2.40)$$

where, R_b is the beam radius, , I_b is the DC beam current. The expression is used for all the intermediate cavities, however ohmic dissipation can be neglected ($Q \rightarrow \infty$) for the output cavity. The equations (2.33) - (2.35) and (2.40) are solved simultaneously with the entry and exit boundary conditions depending on the type of the cavities, i. e., different for closed cavity (intermediate cavities) and for open-ended, waveguide cavity (output cavity) as explained in following subsection. Some others assumptions are adopted to reduce the complexity of the analysis such as: (i) Space-charge effect is neglected in each of the

cavities; (ii) the velocity spread is assumed to be negligible; (iii) cavities are well isolated from each other.

b) Boundary conditions:

If the drift tubes are well below cutoff (as for the case considered in the present work), the boundary conditions for the fields in the driver or buncher cavities are equivalent to those for the closed cavity and are given by [Salop and Caplan (1986)]:

$$h\{\bar{z}_{in}\} = h\{\bar{z}_{out}\} = 0 \quad , \tag{2.41}$$

where, $\bar{z}_{in}$ and $\bar{z}_{out}$ are the z-coordinates at the entrance and exit planes, respectively. The desired solution for the particular cavity is obtained by applying the above boundary condition at the entrance of the cavity and then finding the appropriate values for the real and imaginary parts of the input field profile derivative $dh/d\bar{z}$ which leads to the solution satisfying the boundary condition at the exit of the cavity.

For the output cavity of the device, the entrance boundary condition is the same as for the buncher cavity. However, the exit boundary condition corresponds to the outgoing travelling waves and is given by:

$$\left.\frac{dh}{d\bar{z}}\right|_{\bar{z}=\bar{z}_{out}} = -i\bar{k}_{z_{out}} h\{\bar{z}_{out}\}, \qquad \text{where,} \quad \bar{k}_{\bar{z}_{out}} = \left\langle \beta_{\|0} \right\rangle \left(1 - \bar{k}_{nt}^2 / \bar{\omega}_0^2\right)^{1/2} . \tag{2.42}$$

The boundary conditions on the electron beam at the entrance to the input cavity are described as follows [Salop and Caplan (1986)]:

1) All the ensemble electrons have the same total energy or equivalently the same γ_0.

2) For each specific velocity in the distribution, there are M representative ensemble electrons with a uniform distribution of initial phases given by:

$$\Lambda_{0j} = 2\pi j / M \, , \qquad j = 1, 2, ...M \quad .$$

For each of the cavities following the input cavity, the entrance boundary conditions on the beam correspond to the various components of the beam particle momentum and phases which had evolved for each particle up to that point in the structure. The drift tube section is designed in such a way that no RF field is excited; therefore $f_n = 0$. Hence, for the drift tube section, the equations (2.33) and (2.35) reduce to:

$$\frac{d\,p_t}{d\,\overline{z}} = 0, \quad \text{and} \quad \frac{d\,p_z}{d\,\overline{z}} = 0 \quad . \tag{2.43}$$

Thus, the individual particle momentum, p_t and p_z remain constant in the drift tube section. However, each electron continues to gyrate around the static magnetic field lines, resulting in the phase change and experiences the orbital bunching while passing through the drift tube. Hence, in the drift tube section, equation (2.34) reduces to:

$$\frac{d\Lambda}{d\,\overline{z}} = \overline{\omega}_0 \left[1 - \frac{s\overline{\omega}_c}{\overline{\omega}_0} \frac{\gamma_0}{\gamma} \right] \quad , \tag{2.44}$$

where, the electron relativistic mass factors signify the associated energies, so the ratio of the initial to final electron relativistic mass factor (γ_0 / γ) describes the physics of the electrons' orbital bunching and is critical for the operation of gyroklystron amplifiers.

II. Expressions for the mode amplitude and phase

After getting the equations for the movement of electrons in the interaction structure using Lorentz force equation, now the equations for the RF field growth are derived by using the above derived equations to construct the source term in the governing wave equation. For a *TE* mode, the total transverse electric field is expressed in complex form as:

$$E_t = \sum_{n=1}^{N} A_n\{z,t\}\, e_n\{r,\theta\}\, e^{-i\omega_0 t} \quad . \tag{2.45}$$

The transverse electric field satisfying the wave equation as:

$$\nabla^2 E_t - \frac{1}{c^2}\frac{\partial^2 E_t}{\partial t^2} = \mu_0 \frac{\partial J_t}{\partial t} \quad , \tag{2.46}$$

where, J_t is the transverse AC current density expressed as

$$J_t = J_\omega e^{-i\omega_0 t} \quad ,$$

where, $J_\omega = \int_0^{2\pi} J_t e^{i\omega_0 t} d(\omega_0 t)$ and dS is infinitesimal area element of waveguide's cross section perpendicular to its axis.

On substituting equation (2.45) into equation (2.46), noting that temporal amplitude variation (envelope's) of the sinusoidal RF field is slow when compared to its frequency of oscillation ω_0, i. e., $\frac{\partial A_n}{\partial t} << \omega_0 . A_n$ and integrating over the resonator cross section, we get the following for n^{th} mode.

$$\left[\frac{\partial^2}{\partial z^2} + \frac{\omega_0^2 - \omega_{nc}^2}{c^2} + 2i\frac{\omega_0}{c^2}\frac{\partial}{\partial t}\right] A_n\{z,t\} = -i\mu_0\omega_0 \iint dS\, e_n^* . J_{\omega_0} \quad . \tag{2.47}$$

The intermediate steps being:

$$\nabla^2 E_t = (\nabla_t^2 + \frac{\partial^2}{\partial z^2})E_t = (-k_{nc}^2 + \frac{\partial^2}{\partial z^2})E_t = (-\frac{\omega_{nc}^2}{c^2}E_t + \frac{\partial^2}{\partial z^2})E_t \quad ,$$

and $$\frac{\partial^2}{\partial t^2}[A_n\{z,t\}e^{-i\omega_0 t}] = \left[\frac{\partial^2}{\partial t^2} - 2i\omega_0\frac{\partial}{\partial t} - \omega_0^2\right] A_n\{z,t\}e^{-i\omega_0 t} \quad . \quad .$$

Orthnormality property of the vector functions, expressed below, is also used.

$$\iint e_{m_n l_n} . e^*_{p_n q_n} dS = \delta_{m_n l_n, p_n q_n} \ ,$$

$$\delta_{m_n l_n, p_n q_n} = 1, \quad m_n = p_n \text{ and } l_n = q_n$$

$$\delta_{m_n l_n, p_n q_n} = 0, \quad \text{otherwise.}$$

To obtain slow-time-scale equations, multiply equation (2.47) by A_n^* and multiply the complex conjugate of equation (2.47) by A_n. Then, the resulting two equations are added and subtracted, and integrate the sum or difference over the axial extent of the cavity. The difference leads to:

$$\int_0^L [A_n^* \frac{\partial^2}{\partial z^2} A_n - A_n \frac{\partial^2}{\partial z^2} A_n^* + 2i \frac{\omega_0}{c^2} [A_n^* \frac{\partial}{\partial t} A_n + A_n \frac{\partial}{\partial t} A_n^*]] dz = -i\mu_0 \omega_0 \iiint [A_n^* e_n^* J_{\omega_0} + A_n e_n J_{\omega_0}^*] dS\, dz$$

$$\Rightarrow \int_0^L [A_n^* \frac{\partial^2}{\partial z^2} A_n - A_n \frac{\partial^2}{\partial z^2} A_n^* + 2i \frac{\omega_0}{c^2} |A_n|^2 dz = -i\mu_0 \omega_0 \iiint [A_n^* e_n^* J_{\omega_0} + A_n e_n J_{\omega_0}^*] dS\, dz \quad . (2.48)$$

Similarly, the summation leads to

$$\int_0^L A_n^* \frac{\partial^2}{\partial z^2} A_n + A_n \frac{\partial^2}{\partial z^2} A_n^* + 2 \frac{\omega_0^2 - \omega_{nc}^2}{c^2} A_n A_n^* + 2i[A_n^* \frac{\partial}{\partial t} A_n - A_n \frac{\partial}{\partial t} A_n^*] dz$$

$$= -i\mu_0 \omega_0 \iiint [A_n^* e_n^* J_{\omega_0} - A_n e_n J_{\omega_0}^*] dS\, dz \quad . \qquad (2.49)$$

Integrating $\int_0^L [A_n^* \frac{\partial^2}{\partial z^2} A_n + A_n \frac{\partial^2}{\partial z^2} A_n^*] dz$ by parts leads to $\left(A_n^* \frac{\partial}{\partial z} A_n - A_n \frac{\partial}{\partial z} A_n^* \right)\Big|_0^L$ (2.50)

Similarly, integrating $\int_0^L [A_n^* \frac{\partial^2}{\partial z^2} A_n + A_n \frac{\partial^2}{\partial z^2} A_n^*] dz$, it can be obtained as:

$$(\frac{\partial}{\partial z} |A_n|^2)\Big|_0^L - 2 \int_0^L \left| \frac{\partial}{\partial z} A_n \right|^2 \quad .$$

By choosing only an outgoing wave at $z = L$, i. e.,

$A_n\{z = L, t\} = a_{nL}\{t\} e^{i[k_{nz} z - \psi_n\{t\}]}$, it can be obtained as $(A_n^* \frac{\partial}{\partial z} A_n - A_n \frac{\partial}{\partial z} A_n^*)\Big|_0^L = 2i k_{nz} a_{nL}^2\{t\}$.

$a_{nL}\{t\}$ and $a_n\{t\}$ are related as:

$$a_{nL}\{t\} = \left[\frac{W}{k_{nz} Q_n} \right]^{1/2} \frac{\omega_0}{c} a_n\{t\} \quad . \qquad (2.51)$$

The below steps are followed to arrive at the above relation. $A_n\{z, t\}$ inside the cavity is approximated by the separable form,

$$A_n\{z,t\} = a_n\{t\} \exp i.[-\psi_n\{t\}]\ h_n\{z\} \quad ,$$

$$Q = \frac{\omega_0}{P_{out}} U_{energy} \ , \tag{2.52}$$

where, $U_{energy} = \frac{1}{2}\varepsilon_0 \int_0^L |A_n\{z,t\}|^2 \, dz$, therefore;

$$P_{out} = \frac{1}{2\mu_0 \varepsilon_0} k_{nz} |A_n\{z = L, t\}|^2 = \frac{1}{2\mu_0 \varepsilon_0} k_{nz} a_{nL}^2\{t\} \quad . \tag{2.53}$$

$$Q_n = \frac{\omega_0 \frac{1}{2}\varepsilon_0 W a_n^2\{t\}}{\frac{1}{2\mu_0 \varepsilon_0} k_{nz} a_{nL}^2\{t\}} = \frac{\omega_0 \mu_0 \varepsilon_0^2 W}{k_{nz}} \frac{a_n^2\{t\}}{a_{nL}^2\{t\}} \quad . \tag{2.54}$$

Hence, substituting equation (2.51) into equation (2.50), it can be obtained as:

$$(A_n^* \frac{\partial}{\partial z} A_n - A_n \frac{\partial}{\partial z} A_n^*)\Big|_0^L = 2i k_{nz} a_{nL}^2\{t\} = 2i k_{nz} \frac{W}{k_{nz} Q_n} \frac{\omega_0^2}{c^2} a_n^2\{t\} \quad . \tag{2.55}$$

Then, the difference equation (2.48) can be derived as:

$$\int_0^L [A_n^* \frac{\partial^2}{\partial z^2} A_n - A_n \frac{\partial^2}{\partial z^2} A_n^* + 2i \frac{\omega_0}{c^2} \frac{\partial}{\partial t} |A_n|^2] dz = 2ik_{nz} \frac{W}{k_{nz} Q_n} \frac{\omega_0^2}{c^2} a_n^2\{t\} + 2iW \frac{\omega_0}{c^2} \frac{d}{dt} a_n^2\{t\}$$
$$= -i\mu_0 \omega_0 \int \iint [A_n^* e_n^* J_{\omega_0} + A_n e_n J_{\omega_0}^*] \, dS \, dz \ , \tag{2.56}$$

$$\frac{1}{Q_n} \frac{\omega_0^2}{c^2} a_n^2\{t\} + 4 \frac{\omega_0}{c^2} a_n\{t\} . \frac{d}{dt} a_n\{t\} = -\mu_0 \omega_0 a_n\{t\} . \mathrm{Im}[\frac{i}{W} \iiint [h_n\{z\} e_n^* J_{\omega_0} \exp i[\psi_n\{t\}]] dS dz \ . \tag{2.57}$$

Thus, we arrive at differential equation governing mode amplitude:

$$\frac{d}{dt} a_n\{t\} + \frac{\omega_0}{2Q_n} a_n\{t\} = -\frac{1}{2\varepsilon_0} . \mathrm{Im}[\frac{i}{W} \int \iint [h_n\{z\} e_n^* J_{\omega_0} \exp i[\psi_n\{t\}]] \, dS \, dz \quad . \tag{2.58}$$

Substituting the below expressions in the summation equation (2.49),

$$[A_n^* \frac{\partial}{\partial t} A_n - A_n \frac{\partial}{\partial t} A_n^*] = -2i h_n^2\{z\}.a_n^2\{t\}\frac{d}{dt}\psi_n\{t\} \ , \tag{2.59}$$

$$\int_0^L \left|\frac{\partial}{\partial z} A_n\right|^2 dz = a_n^2\{t\}\int_0^L \left|\frac{d\, h_n}{d\, z}\right|^2 dz = 0 \quad . \tag{2.60}$$

if h_n is assumed symmetrical, as is the case now $(\frac{\partial}{\partial z}|A_n|^2)\Big|_0^L = 0$, since $A_n \to 0$ at the input of cavity and $|A_n|$ = constant at the output of cavity, hence one can get the expression:

$$\int_0^L [2\frac{\omega_0^2 - \omega_{nc}^2}{c^2}.a_n^2\{t\}h_n^2\{z\} + 4\frac{\omega_0}{c^2}[a_n^2\{t\}h_n^2\{z\}\frac{d}{dt}\psi_n\{t\}]]\, dz$$

$$= -2\mu_0\omega_0 a_n\{t\}\mathrm{Re}\left[i\int\iint[h_n\{z\}e_n^* J_{\omega_0}\exp i[\psi_n\{t\}]]\, dS\, dz\right] \quad . \tag{2.61}$$

Approximating $\omega_0^2 - \omega_{nc}^2$ as $2\omega_0(\omega_0 - \omega_{nc})$, we get

$$[4\frac{\omega_0(\omega_0 - \omega_{nc})}{c^2}.a_n^2\{t\}h_n^2\{z\} + 4\frac{\omega_0}{c^2}[a_n^2\{t\}h_n^2\{z\}\frac{d}{dt}\psi_n\{t\}]]\int_0^L h_n^2\{z\}\, dz$$

$$= -2\mu_0\omega_0 a_n\{t\}\mathrm{Re}[i\int\iint[h_n\{z\}e_n^* J_{\omega_0}\exp i[\psi_n\{t\}]]\, dS\, dz] \quad , \tag{2.62}$$

$$[4\frac{\omega_0(\omega_0 - \omega_{nc})}{c^2}.a_n^2\{t\}h_n^2\{t\} + 4\frac{\omega_0}{c^2}[a_n^2\{t\}h_n^2\{z\}\frac{d}{dt}\psi_n\{t\}]]$$

$$= -2\mu_0\omega_0 a_n\{t\}\mathrm{Re}\left[\frac{i}{W = \int_0^L h_n^2\{z\}\, dz}\int\iint[h_n\{z\}e_n^* J_{\omega_0}\exp i[\psi_n\{t\}]]\, dS\, dz\right] \quad . \tag{2.63}$$

The differential equation governing phase of the mode can be written as:

$$\frac{d}{dt}\psi_n\{t\} + \omega_0 = \omega_{nc} - \frac{1}{2\varepsilon_0 a_n\{t\}}\mathrm{Re}\left[\frac{i}{W}\int\iint[h_n\{z\}e_n^* J_{\omega_0}\exp i[\psi_n\{t\}]]\, dS\, dz\right] \tag{2.64}$$

Therefore, the normalized RF field amplitude and phase can be obtained from equations (2.65) and (2.66) as [Fliflet *et al*. (1991)]:

$$\frac{d f_n}{d \tau} = -\frac{f_n}{2Q_n} + \bar{I}_n \int_0^L d\bar{z}\, h\{\bar{z}\} \left\langle J_s'\{k_{nt} r_L\} \frac{p_t}{p_z} \cos\left[\left[\Lambda + \bar{\psi}_n\right] + \left(m_n - s\right)\theta_0\right] \right\rangle_{\Lambda_0, \theta_0} \quad , \quad (2.65)$$

and $$\frac{d\psi_n}{d\tau} = -\frac{\omega_0 - \omega_{n0}}{\omega_0} - \bar{I}_n \int_0^L h\{\bar{z}\}\, d\bar{z}. \left\langle J_s'\{k_{nt} r_L\} \frac{p_t}{p_z} \sin\left((\Lambda + \bar{\psi}_n) + \left(m_n - s\right)\theta_0\right) \right\rangle_{\Lambda_0, \theta_0} . \quad (2.66)$$

I_n is the normalization current given by:

$$I_n = \frac{|e| Z_0}{m_e c^2 \bar{\omega}_0} \frac{J_{m_{n-s}}^2 \{k_{nt} R_b\}}{\pi \left(1 - m_n^2 / x_{m_n l_n}'^2\right) J_{m_n}^2 \left\{x_{m_n l_n}'^2\right\} \bar{W}} I_b \quad . \quad (2.67)$$

Hence, the mechanism of beam-wave interaction in the gyroklystron amplifier is analyzed by solving the coupled nonlinear differential equations describing the electron momentum and phase equations (2.33) - (2.35) and the coupled time-dependent equations describing the mode amplitude and phase equations (2.65) - (2.66). These equations are then solved self-consistently for each cavity by satisfying the appropriate boundary conditions for the particle momentum and phases and the field profile. Hence, in the present developed analysis for the gyroklystrons, the momentum and phase are obtained for each cavities of the gyroklystron amplifier such that the particle momentum and phases entering the adjacent cavity are considered as those at the exit of the first cavity except for the phase change which mainly occurs in the field-free drift tube.

III. Time-dependent RF output power and electronic efficiency

The mode amplitude f_n at each time step is calculated using equation (2.65). The power transfer from the electrons to the n^{th} mode in the cavity at each time step is given by [Fliflet *et al*. (1991)]:

$$P_n\{\tau\} = \frac{\pi m_e^2 c^4}{2 Z_0 \left|e^2\right|} \frac{(1 - m_n^2 / x_{m_n l_n}'^2) J_{m_n}^2 \{x_{m_n l_n}'\}}{Q_n J_{m_n - s}^2 \{k_{nt} R_b\}} \bar{\omega}_0 \bar{W} \left| f_n\{\tau\} \right|^2 \quad . \quad (2.68)$$

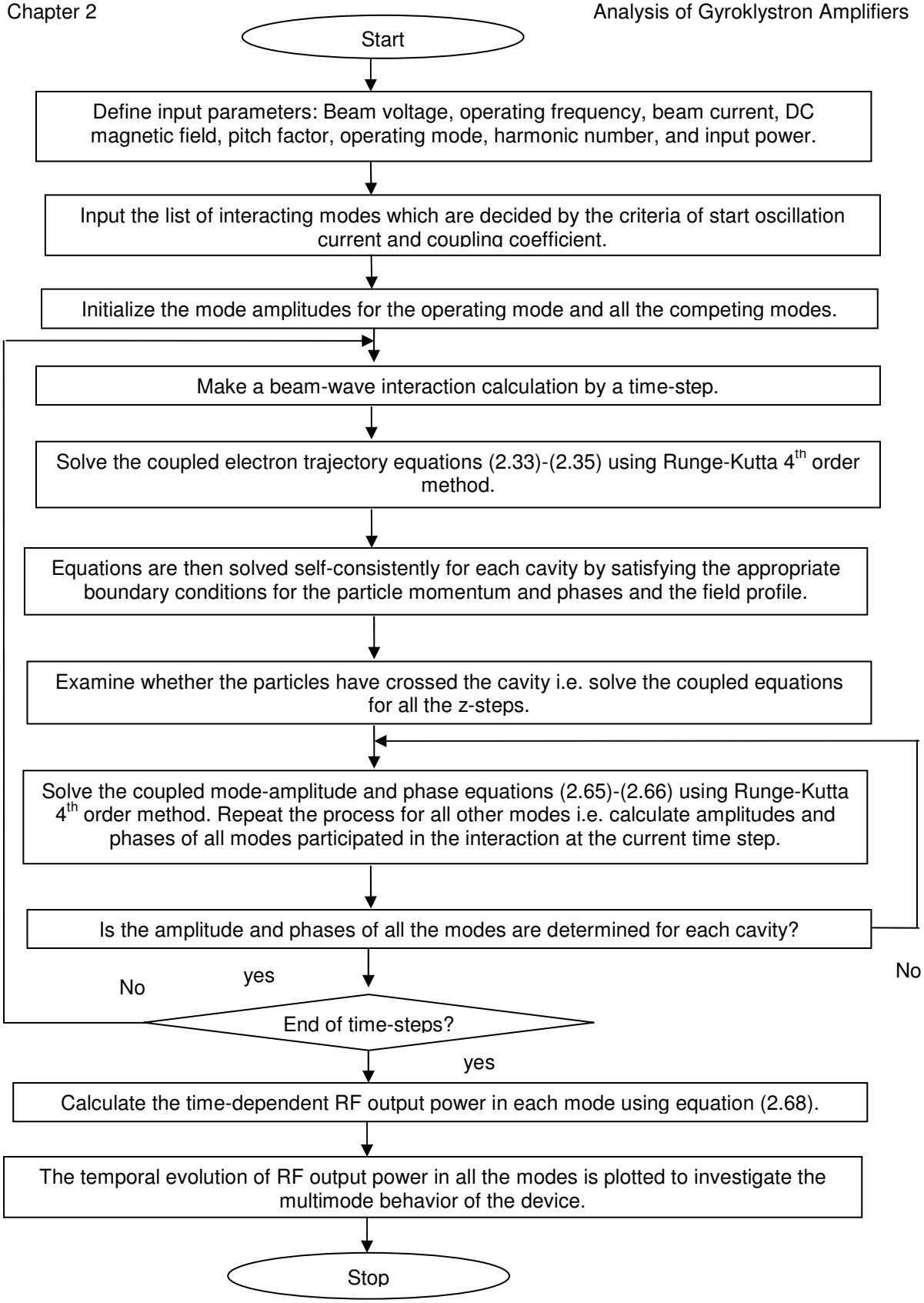

Figure. 2.2: Flow chart for time-dependent multimode analysis of gyroklystron.

The electronic efficiency (η_{el}) can be determined as the difference between the initial energy and the final energy of electrons, which can be expressed in terms of the relativistic mass factor as:

$$\eta_{el} = \frac{\gamma_0 - \langle \gamma(z=L) \rangle_{\Lambda_0,\theta_0}}{\gamma_0 - 1} = \frac{\gamma_0 \beta_{\perp 0}^2}{2(\gamma_0 - 1)} \eta_{\perp} \quad . \tag{2.69}$$

2.3. Numerical Benchmarking

Based on the analytical method described above, a time-dependent, multimode nonlinear analysis for a gyroklystron amplifier is performed to examine the RF behavior of the overmoded cavity in the gyroklystron amplifier. A computer friendly numerical code is written to analyze the beam-wave interaction mechanism in the gyroklystron amplifier. In the present analysis, the coupled differential equations solving electron momentum and phase and the time-dependent coupled differential equations solving mode amplitude and phase are solved using fourth order Runge-Kutta method. This code provides the comprehensive picture of the multimode effect on the performance of the device. The flow chart showing the step-by step procedure of the multimode analysis carried out for performance evaluation is shown in Fig. 2.2.

2.3.1. Three-Cavity, Second Harmonic Gyroklystron Amplifier

Moreover, the developed multimode analysis as described above has been validated with the recently reported experimental results of a 32.3GHz three-cavity, second harmonic gyroklystron amplifier operating in the TE_{02} mode [Antakov *et al*. (2011)]. In order to reduce the magnetic field requirement, the higher harmonic amplifier is considered. But the efficiency decreases with the harmonic number, hence the presented study is limited to second harmonic gyroklystron amplifiers. Table 2.1 shows the design specifications considered for the multimode analysis of the device.

Table. 2.1: Design parameters for 32.3GHz, second harmonic, three-cavity gyroklystron amplifier [Antakov *et al*. (2011)].

Parameters	Specifications
Operating Mode	TE_{02}
Beam Voltage (V_b)	70kV
Beam Current (I_b)	20A
Velocity Pitch Factor (α)	1.1
Beam radius (R_b)	$0.43R_w$
DC Magnetic Field (B_0)	0.656T
Input Cavity Length	16mm
Buncher Cavity Length	15mm
Output Cavity Length	22.3mm
Quality factor of input cavity (Q_1)	600
Quality factor of buncher cavity (Q_2)	450
Quality factor of output cavity (Q_3)	1050

2.4. Results and Discussion

2.4.1. Mode Selection and Stability Analysis

The mode selection and stability analysis has been done as an initial study which signifies the selection of competing modes that affect the operating mode and device performance. It includes the calculation of the two important parameters coupling coefficient and the start oscillation current.

2.4.1a Coupling coefficient

The coupling coefficient is a measure of the coupling of the electron beam to the RF mode in the cylindrical cavities and is given by the expression:

$$H_{m_n l_n} = \frac{J^2_{m_n \pm s}\{k_{nt} R_b\}}{(x'^2_{m_n l_n} - m_n^2) J^2_{m_n}\{x'_{m_n l_n}\}} \quad . \tag{2.71}$$

By choosing the optimum ratio of electron beam to cavity radius, the coupling coefficient is maximum for the selected mode so that the desired mode is excited and other competing modes are suppressed.

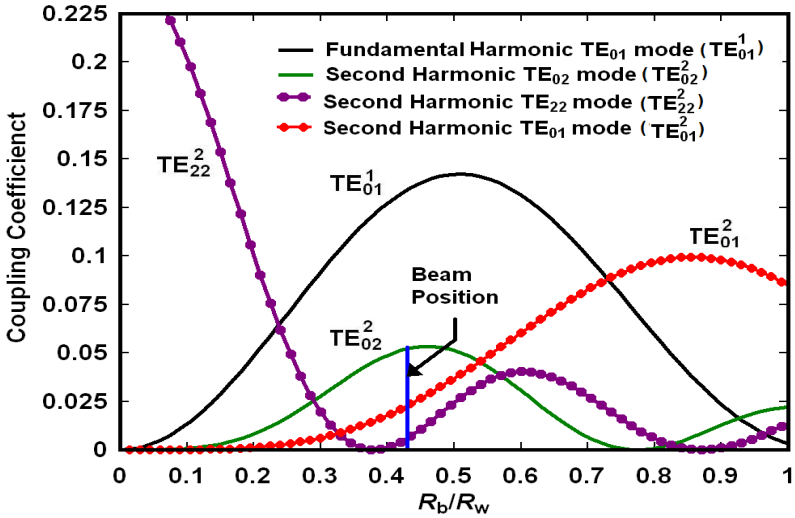

Figure. 2.3: Coupling coefficient as a function of ratio of beam to waveguide radius (R_b/R_w) for operating TE_{02}^2 mode and possible competing modes.

Figure 2.3 shows the plot of the coupling coefficient for various modes as a function of the normalized beam radius. The first radial maximum of the TE_{02}^2 mode which is equal to the normalized beam radius of 0.43 is the normalized beam position for the maximum TE_{02}^2 interaction (the superscripts in the nomenclature of modes refer to the s^{th} harmonic interaction number). The value of R_b / R_w=0.43 reduces the interaction strength of possible competing modes and hence is used to limit the parasitic modes oscillation.

2.4.1b Start oscillation current

One of the important characteristic for the effective operation of a gyroklystron amplifier is the start oscillation current criteria study which signifies that the operating current should be less than the start oscillation current. It is also important to estimate the start oscillation current of various possible competing modes.

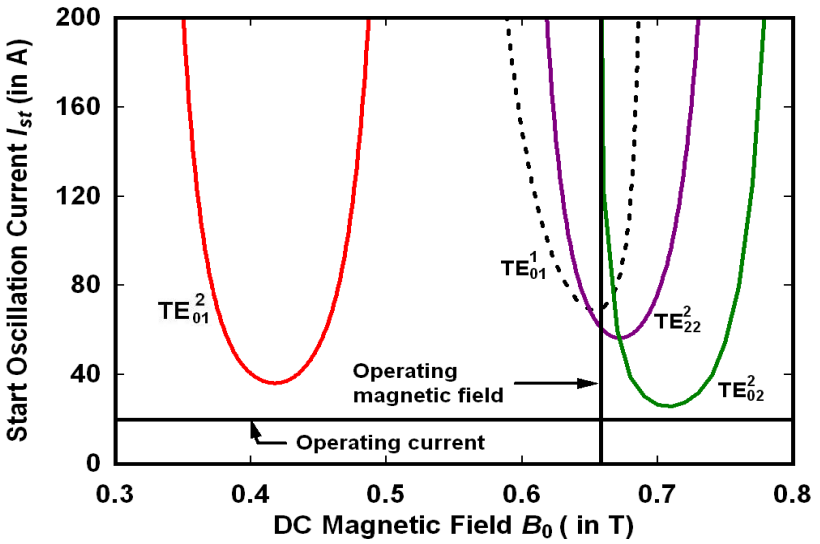

Figure. 2.4: Start oscillation current for operating second harmonic mode and possible competing modes as a function of DC magnetic field in the input cavity, where the operating point $B_0 = 0.656$T and I_b = 20A is indicated.

By calculating and comparing the start oscillation current of desired and competing modes, it is ensured that the desired mode is excited with maximum efficiency at the desired power level, thus suppressing the unwanted modes. The normalized start oscillation current in terms of normalized interaction length *(μ)* and detuning (Δ) is given by:

$$I_{st} = \left(\frac{\pi}{2}\right)^{5/2} \frac{c^3 m_e \varepsilon_0}{e} \left(\frac{2^s s!}{s^s}\right) \frac{\beta_{\perp 0}^{-2(3-s)} \gamma_0}{Q} \frac{L}{\lambda} \frac{(4/\pi\mu^2)\,[e^{2x^2}/(\mu x - s)]}{H_{m_n l_n}} \quad . \qquad (2.72)$$

The start oscillation current in Fig. 2.4 is calculated for the operating TE_{02}^2 mode and the nearby competing modes for a 32.3GHz gyroklystron amplifier as a function of DC magnetic field (B_0) in the input cavity. By considering the experimental value of the DC magnetic field of 0.656T, the start oscillation current (I_{st}) for the desired TE_{02}^2 mode in the input cavity is obtained as around 100A which is much larger than the operating current 20A, thus ensuring the stable operation of the gyroklystron as an amplifier. Further, it has been observed from Fig. 2.4 that the possible competing modes TE_{22}^2, TE_{01}^2 and TE_{01}^1 are suppressed as the device operating current is much lower than the start oscillation current

over the entire possible range of DC magnetic field B_0.

2.4.2. Time-Dependent Multimode Analysis

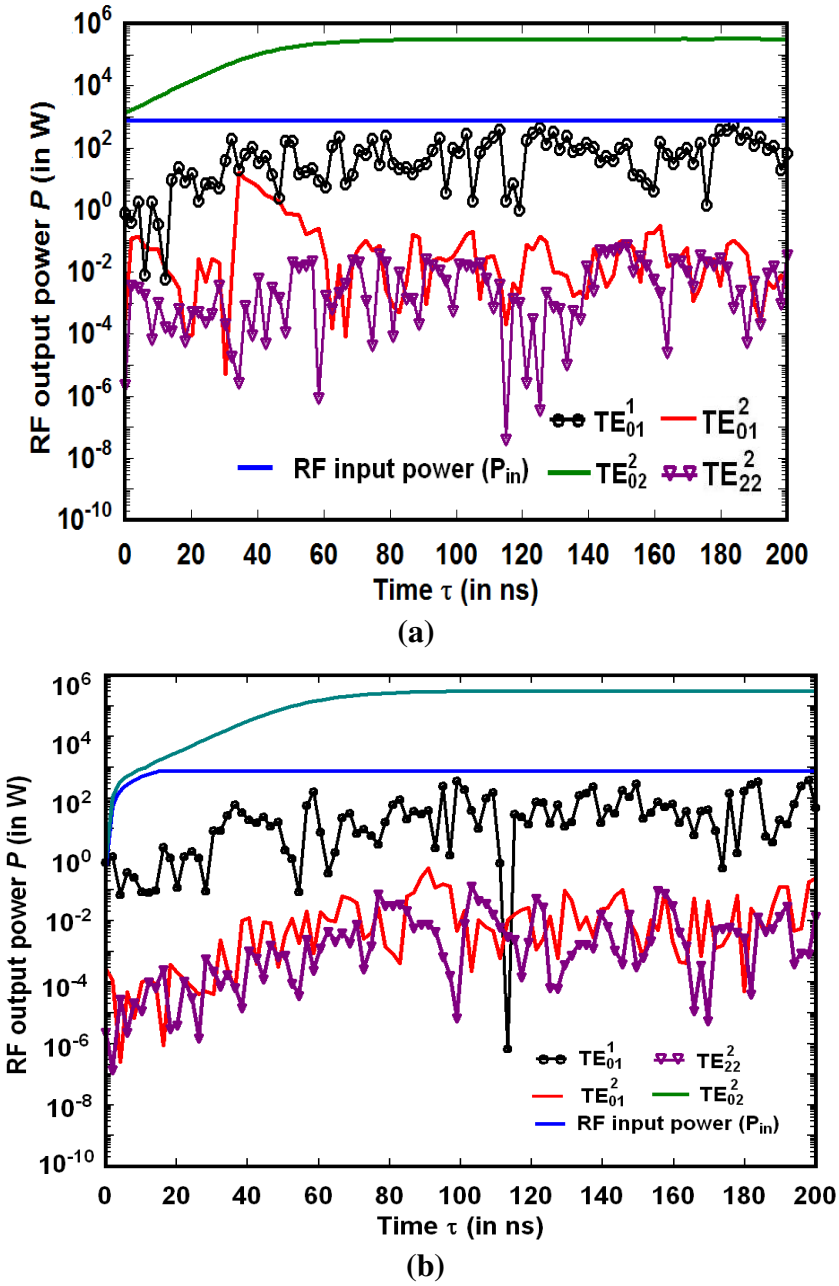

Figure. 2.5: Temporal evolution of RF output power in the different modes in the output cavity of the operating TE_{02}^{2} mode **(a)** for a constant RF input power P_{in} =0.75kW, **(b)** for a ramped RF input power.

For the design parameters shown in Table 2.1, the time-dependent self-consistent multimode analysis as explained in subsection 2.2.1 is carried out.

To obtain the analytical results equivalent to the real-time simulation model, the ramped RF input in the operating TE_{02}^{2} mode is considered as shown in Fig. 2.5(b). It is worth mentioning that in the case of simulation as well as for the experimental analysis, the RF input power is coupled to the RF input cavity of the device through an appropriately designed coupler where more than 95% of the power is transmitted in the operating TE_{02}^{2} mode. But in the case of analysis, the RF input power is directly coupled in the main mode whereas competing modes are assumed to be noise. The amplitude of RF input power (P_{in}) is increased eventually from 0.5W to 750W in the period $0 < \tau < 15$ ns. When $\tau > 15$ns, the constant amplitude of 750W RF input power is considered. In the beginning, the RF output power in the operating TE_{02}^{2} mode begins to grow slowly and after 15ns, the beam interacts with the saturated RF input power. The interaction reaches the steady state at around 100ns. The RF output power corresponding to the TE_{02}^{2} mode eventually dominates all competing modes, and the mode competition is observed mainly due to the fundamental harmonic TE_{01}^{1} mode. The saturated RF output power is obtained as ~ 319kW in the operating TE_{02}^{2} mode and ~10W in the TE_{01}^{1} mode. The gain (in dB) of the device is given by the ratio of the saturated RF output power (~319kW) to the saturated RF input power (0.75kW) and is obtained as ~26.3dB. The saturated RF output power corresponding to other competing TE_{01}^{2} and TE_{22}^{2} modes is around 0.01W and 0.001W, respectively.

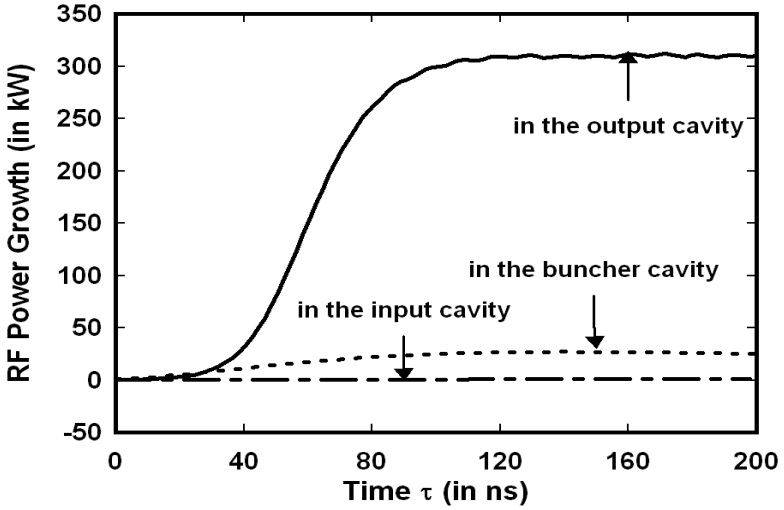

Figure. 2.6: Temporal evolution of RF power in the input, buncher and output cavities.

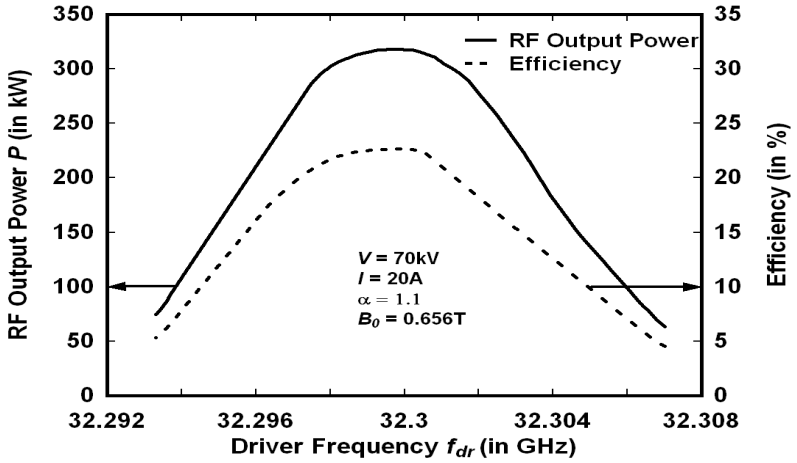

Figure. 2.7: RF output power and efficiency as a function of driver frequency.

Figure 2.6 shows the evolution of RF power in all the cavities with time. It is quite evident from Fig. 2.6 that the RF power growth is small in the input cavity since the energy exchange between the RF field and the electron beam is much smaller in the cavity. However, in the buncher and the output cavity, the electron beam continues to be velocity modulated for the bunching process and RF field amplification occurs. The strong beam-wave interaction is observed in the output cavity, producing saturated output power ~319kW in the desired TE_{02}^{2} mode at around 100ns.

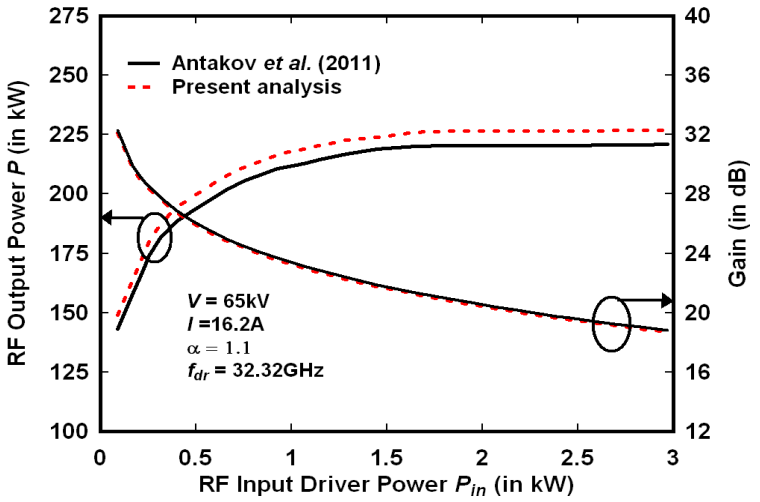

Figure. 2.8: RF output power and gain as a function of driver power.

The bandwidth and gain of the device are computed by plotting the variation of RF output power with frequency and RF driver power. Figure 2.7 shows the variation of RF output power and efficiency with frequency. It is evident from the figure that the RF output power ~319kW is obtained at the center frequency of 32.3GHz. The 3dB bandwidth obtained through the present analysis is ~0.027% (8MHz). Figure 2.8 shows the comparison of the reported experimental results [Antakov *et al.* (2011)] with the analytically obtained results for the dependence of RF output power and gain on RF input driver power. The saturated RF output power is obtained as ~227kW corresponding to ~19.54dB gain. The analysis was carried out for a beam voltage of 65kV, beam current 16.2A and center frequency of 32.32GHz. The computed results obtained are in agreement (within 10%) with the reported experimental results.

2.4.3. Sensitivity Analysis

The effect of various parameters such as beam voltage, beam current and beam pitch factor have been studied to investigate the sensitivity of device performance to these parameters.

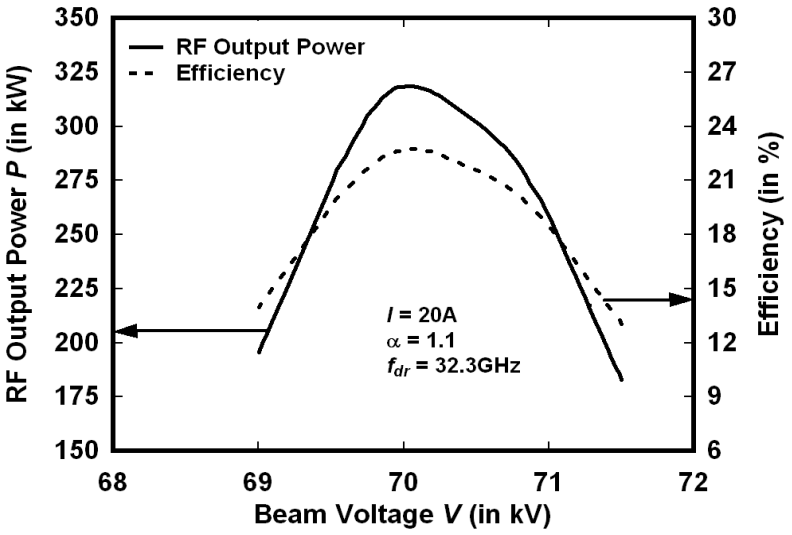

Figure. 2.9: RF output power and efficiency as a function of beam voltage.

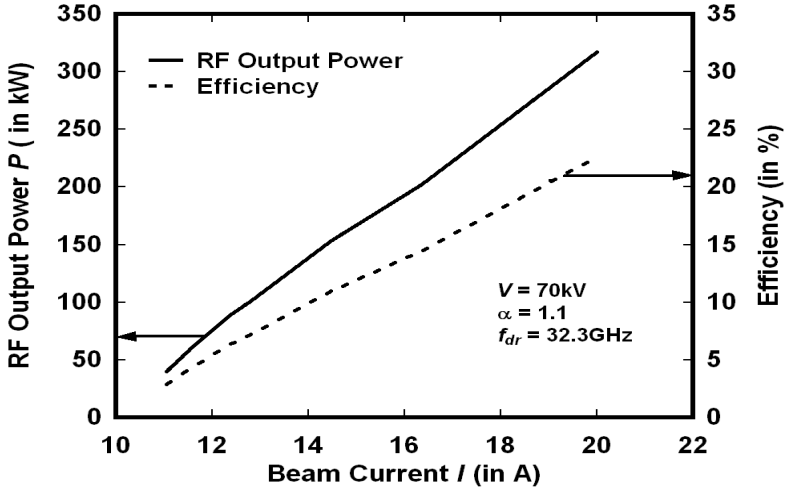

Figure. 2.10: RF output power and efficiency as a function of beam current.

Figure 2.9 shows the variation of RF output power and efficiency with beam voltage for a 20A electron beam with α = 1.1. It is observed that the maximum RF output power ~319kW and efficiency ~ 23% are obtained at the beam voltage of 70kV. Figure 2.10 shows the dependence of RF output power and efficiency on beam current for a 70kV electron beam with α=1.1. It can be seen that the RF output power and efficiency increase with the increase in the beam current which is mainly due to the enhancement in the beam energy for beam-wave interaction. As seen from the Fig. 2.10, the RF output power

~319kW and efficiency ~23% are obtained at a beam current of 20A. Then, the RF output power decreases for higher values of beam current due to the operation of the device near the start oscillation current.

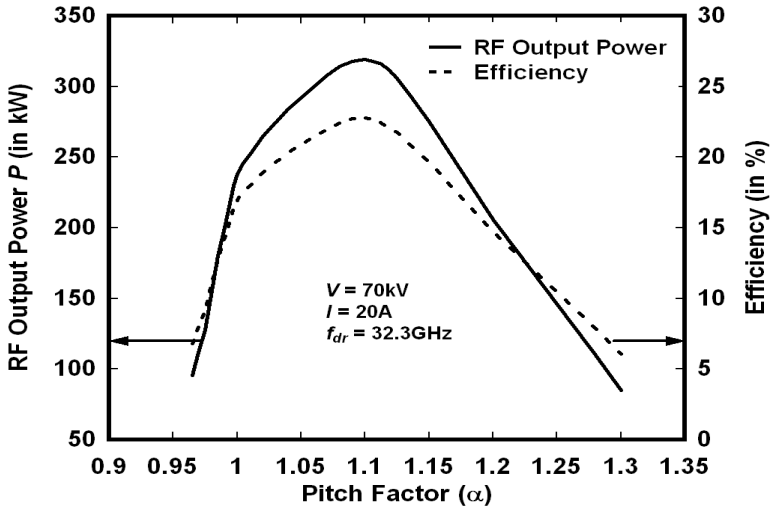

Figure. 2.11: RF output power and efficiency as a function of beam pitch factor.

In Fig. 2.11, the dependence of the RF output power on the electron beam pitch factor is shown for a 70kV, 20A electron beam. The maximum output power is achieved at a pitch factor ~1.1. The decrease in both RF output power and efficiency has been observed for higher and lower values of the electron-beam pitch factor.

2.5. Conclusion

Review of the generalized linear and nonlinear analysis of the gyroklystron has been presented. In the present chapter, a self-consistent, time-dependent, multimode nonlinear analysis has been developed to investigate the beam-wave interaction behavior in an overmoded cavity operation of the gyroklystron amplifier. The developed analysis incorporates the effect of all nearby competing modes on the device performance, hence provides a realistic scenario to determine the accurate output power and efficiency in each mode. The generalized coupled nonlinear equations of motion of electrons are used for the

calculation of momentum and phase of the particles by considering the cumulative effect of all possible modes. The field-profile in each of the cavities is calculated self-consistently using the modified Vlasov equation. Coupled time-dependent equations are solved to calculate the mode amplitude and phase in each cavity at each time step. A flowchart explaining the step-by-step procedure for the multimode analysis is also shown. A numerical code has been written based on the developed analysis and further benchmarked for the performance evaluation of the reported experimental three-cavity Ka-band second harmonic gyroklystron amplifier. The linear analysis has been used for calculating the initial device design parameters, like coupling coefficient, start oscillation condition which provides the device design in terms of the beam radius, beam current and magnetic field corresponding to the operating mode along with the other possible competing modes. It is assumed that all electrons have the same transverse velocity so that effects due to spreads in the spatial and velocity distribution are neglected. For simplification, space-charge effect is also neglected. From the developed analysis, the temporal evolution of the RF output power in all the modes is plotted and observed saturated RF output power of 319kW in the operating TE_{02} mode. The mode competition is mainly due to fundamental harmonic TE_{01} mode. The analytical results obtained are then benchmarked with the reported experimental values and found to be in close agreement. The parametric effects have been presented to show the device sensitivity in terms of output power with the beam parameters which further helpful in optimizing the design parameters. The effect of frequency and gain variation on the RF output power has been studied to estimate the bandwidth and gain of the device. The gain and bandwidth of the device has been obtained as ~26.3dB and 8MHz, respectively. The analysis developed here will be further used in the subsequent chapters for the design and performance improvement studies of the gyroklystron amplifier.